Ringing Suppression of SiC MOSFET Using a Strongly Coupled External Resonator Through Analogy With Passive PT-Symmetry

Kenichi Yatsugi, Koshi Oishi, and Hideo Iizuka, *Member, IEEE*

***Abstract*—Suppressing parasitic ringing, unwanted oscillation caused by switching, sufficiently and reliably, is of great importance in wide bandgap semiconductor devices. *RC*-circuits inserted in parallel with switching devices have been widely used to suppress such parasitic ringing in power electronics circuits due to simple configurations. However, short-circuit current would flow through power lines if capacitors are broken. In this article, we show that parasitic ringing can be damped with an external *RLC* resonator implemented in parallel to a bus bar. The configuration enables the strong magnetic coupling, which results in high ringing suppression effect. Moreover, the external resonator is designed through analogy with passive parity-time (PT) symmetry. In the range of unbroken phase, ringing energy is distributed effectively to the external resonator, and the damping rate is increased by increasing the loss of the external resonator. Our results represent a significant step toward practical applications of passive PT-symmetry.**

***Index Terms*—Electromagnetic interference, MOSFETs, silicon carbide, snubbers, switching circuits, wide band gap semiconductors.**

I. Introduction

POWER electronics plays a crucial role in wide range of industrial electronics systems such as electric, hybrid, and fuel cell vehicles, railways, and renewable energy [1]–[4]. Wide bandgap semiconductor devices, such as silicon carbide (SiC) MOSFETs (metal-oxide-semiconductor field-effect transistors) and gallium nitride (GaN) high electron mobility transistors have been expected to offer high speed switching, enabling high efficiency or high-power density of power converters [5]–[9]. On the other hand, unwanted oscillations caused by parasitic inductances and capacitances, which are called "ringing," become more severe with increasing the switching speed [10]–[13]. Ringing causes electromagnetic interference [14]–[16].

RC-circuits, which are called as snubber circuits, have been traditionally used to suppress ringing due to simple passive configurations and its effectiveness. Inserting capacitors and resisters in parallel with switching devices damps the ringing [10], [17]–[19]. In *RC*-circuits, ceramic capacitors are often used due to high capacitances [17], [20], [21]. However, short-circuit current would flow through power lines if capacitors are broken [20], [22], [23]. Thus, alternative approach is desired to avoid the insertion of ceramic capacitors in parallel with switching devices while suppressing ringing effectively.

Recently, non-Hermitian parity-time (PT) symmetry, arising from quantum mechanics, has been expanded to various fields of technology, such as photonics [24], [25], acoustics [26], [27] and electronics [28]–[30]. Especially, practical applications of PT-symmetry in electronics have been reported very recently [30]. Typical PT-symmetry systems consist of resonators with the same resonance frequency, and balanced gain and loss. In such a system, eigen values and eigen modes coalesce at an exceptional point, and in the unbroken phase, energy is equally distributed between loss and gain resonators [25], [30]. Moreover, PT-symmetry can be expanded to passive systems, which is called passive PT-symmetry [25]. At first, passive PT-symmetry was observed as loss induced transparency in a coupled lossy and lossless waveguide system [31]. As in the case of PT-symmetry, energy in passive PT-symmetry is equally distributed among resonators in unbroken phase [31], [32]. The important suggestion of passive PT-symmetry is that in a coupled lossy and lossless resonator system, energy is distributed effectively between resonators and the total energy damping increases as increasing the loss of the lossy resonator in the range of unbroken phase [31].

In this article, we show that parasitic ringing can be significantly suppressed with a magnetically coupled external *RLC* resonator. The magnetic coupling is realized by implementing the external resonator in parallel to a bus bar of the main circuit. Such configuration needs no circuit-element inserted in parallel with switching devices, hence the reliability is ensured. The external resonator is designed through analogy with passive-PT symmetry. In the range of unbroken phase, ringing energy is distributed effectively to the external resonator, and the damping rate is increased as increasing the loss of the external resonator. Recently, a scheme for ringing suppression using a magnetically coupled external resonator consisting of a thin printed circuit board (PCB) Rogowski coil has been proposed [33]. Our approach is distinctively different from the report in the following two features. The first feature is a strong coupling scheme between resonators. While such a PCB Rogowski coil

Manuscript received May 20, 2020; revised July 15, 2020; accepted July 27, 2020. Date of publication August 3, 2020; date of current version October 30, 2020. Recommended for publication by Associate Editor A. Lindemann. *(Corresponding author: Kenichi Yatsugi.)*

Kenichi Yatsugi and Koshi Oishi are with the Toyota Central Research and Development Laboratories Inc., Nagakute 480-1192, Japan (e-mail: yatsugi@mosk.tytlabs.co.jp; e1616@mosk.tytlabs.co.jp).

Hideo Iizuka is with the Toyota Research Institute North America, Ann Arbor, MI 48105 USA (e-mail: hideo.iizuka@toyota.com).

Color versions of one or more of the figures in this article are available online at https://ieeexplore.ieee.org.

Digital Object Identifier 10.1109/TPEL.2020.3013399

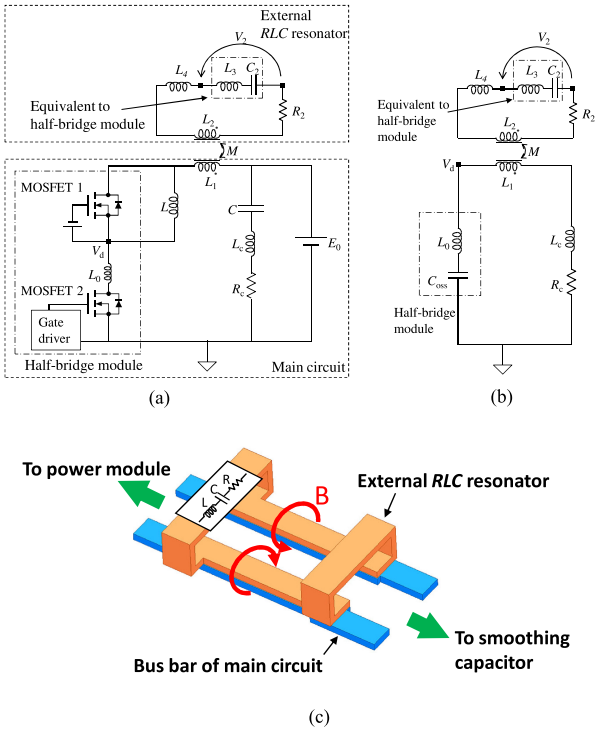

Fig. 1. Circuit configuration. (a) Double-pulse circuit with an external resonator. (b) High-frequency circuit. (c) Schematic of the magnetically coupled bus bar.

can be inserted even in a narrow space, strong magnetic coupling between a Rogowski coil and the main circuit in high frequency is often limited because coupling strength and bandwidth of a Rogowski coil are in a tradeoff relationship [34]–[37]. Strong coupling using a Rogowski coil can be realized by increasing the turn number or cross-section area, resulting in increasing the self-inductance which lowers the resonance frequency. On the other hand, our configuration promises high resonant frequency due to its small self-inductance and realizes strong magnetic coupling. Second feature is physical insight for optimal design in our system. We elucidate how ringing is optimally damped using passive PT symmetry theory. The notable point is that the analogy of passive PT symmetry can be applied to strongly-coupled highly-lossy systems. So far, passive PT symmetry is observed in weakly-coupled less-lossy systems [31], [38]. Although the intrinsic damping rate of the external resonator and coupling coeffcient are large, our system can be treated with passive PT-symmetry analogy.

II. Circuit Design

A. Circuit Configuration

We employed an inductive-load double-pulse test circuit shown in Fig. 1(a) to evaluate the ringing behavior [10], [17]. The circuit consists of two pairs of a SiC MOSFET and a freewheel diode included in a half-bridge module, load inductor L, smoothing capacitor C, and voltage source E_0. The external resonator is magnetically coupled via the mutual inductance of bus bars M. L_1, L_0, and L_c are the parasitic inductances of the bus bar of the main circuit, the module, and the smoothing capacitor, respectively. R_c is the equivalent series resistance of the circuit. L_2 is the inductance of the bus bar of the external resonator. L_3 is the inductance equivalent to that of the half-bridge module of the main circuit. L_4 is the inductance for adjustment.

The ringing can be analyzed with the high-frequency equivalent circuit shown in Fig. 1(b) because the ringing phenomenon is described by a resonance between the output capacitances of the switching device and parasitic inductances [10], [17]. $C_{\rm oss}$ is the output capacitance of MOSFET. Then, we designed the external resonator using $C_2 = C_{\rm oss}$ and $L_2 + L_3 + L_4 = L_0 + L_1 + L_c$. Thus, our system is considered as magnetically coupled *RLC* resonators having the same resonance frequency. When $R_c \ll \sqrt{(L_0 + L_1 + L_{\rm c})/C_{\rm oss}}$, R_2, the main circuit and the external resonator can be regarded as lossless and lossy resonators, respectively.

The external resonator is magnetically coupled by mounting the bus bar of the external resonator alongside the bus bar of the main circuit, as shown in Fig. 1(c). The external resonator is insulated from the main circuit by using Kapton tapes. The bus bars of the main circuit and the external resonator are wrapped by Kapton tapes and then put together with double sided Kapton tapes. Surface mount ceramic capacitors, inductors, and resistors were used for C_2, L_3, L_4, and R_2.

B. Coupled Mode Theory

We start with reviewing coupled mode theory (CMT) for considering a system consisting of two coupled resonators [25], [41]. We assume that the two resonators have the damping rates γ_1, γ_2 ($0 < \gamma_1 < \gamma_2$), and the same resonance frequency $\omega_{\rm o}$. Using the $\exp(i\omega t)$ convention, the system dynamics is described as

$$-i\frac{d}{dt}\begin{bmatrix} A_1 \\ A_2 \end{bmatrix} = \begin{bmatrix} \omega_0 + i\gamma_1 & \kappa \\ \kappa & \omega_0 + i\gamma_2 \end{bmatrix}\begin{bmatrix} A_1 \\ A_2 \end{bmatrix}. \tag{1}$$

where A_1 and A_2 are the mode amplitudes, and κ is the coupling rate. In this configuration, PT-symmetry is re-established by applying gauge transformation

$$\begin{bmatrix} A_1 \\ A_2 \end{bmatrix} = e^{-\chi t}\begin{bmatrix} A'_1 \\ A'_2 \end{bmatrix} \tag{2}$$

where $\chi = (\gamma_1 + \gamma_2)/2$. Then, (1) is rewritten as

$$\begin{aligned} -i\frac{d}{dt}\begin{bmatrix} A'_1 \\ A'_2 \end{bmatrix} &= \begin{bmatrix} \omega_0 + i\gamma_1 & \kappa \\ \kappa & \omega_0 + i\gamma_2 \end{bmatrix}\begin{bmatrix} A'_1 \\ A'_2 \end{bmatrix} - i\chi\begin{bmatrix} A'_1 \\ A'_2 \end{bmatrix} \\ &= \begin{bmatrix} \omega_0 - \frac{i(\gamma_2-\gamma_1)}{2} & \kappa \\ \kappa & \omega_0 + \frac{i(\gamma_2-\gamma_1)}{2} \end{bmatrix}\begin{bmatrix} A'_1 \\ A'_2 \end{bmatrix}. \end{aligned} \tag{3}$$

In the CMT for a series *RLC* resonator, the resonant frequency $\omega_{\rm o}$, the damping rate γ_n, and the coupling rate κ are expressed as $\omega_0 = 1/\sqrt{L_n C_n}$, $\gamma_n = (\omega_0 R_n\sqrt{C_n/L_n})/2$, and $k = \omega_0/2Q$, respectively. $\mu = M/\sqrt{L_1 L_2}$ is the magnetic coupling coefficient, where M and L_n ($n = 1, 2$) are mutual-inductance and self-inductance. In the 2×2 matrix in Eq. 3, the diagonal elements have the same magnitude and opposite sign in the imaginary part. So, this system is considered as a PT symmetric system with global exponential decay. Such system has a phase

transition point so-called *exceptional point*, where two eigen values and eigen modes coalesce. The exceptional point meets

$$\gamma_2 - \gamma_1 = 2\kappa. \tag{4}$$

Here, we consider that resonator 1 is excited. Below the exceptional point, so-called *exact phase*, the energy of each resonator is continuously exchanged, and the total loss increases as increasing γ_2 [31]. Above the exceptional point, through passive PT symmetry braking, the energy exchange is reduced and as the result, the total energy loss is reduced with increasing γ_2 [31]. Therefore, ringing suppression is maximized at the exceptional point, and the damping rate of the external resonator is derived

$$\gamma_2 = \gamma_1 + 2\kappa = \frac{\omega_0}{2}\left(R_1\sqrt{\frac{C_1}{L_1}} + 2\frac{M}{\sqrt{L_1 L_2}}\right). \tag{5}$$

C. Circuit Equations

As discussed earlier, the maximum damping rate is achieved at the exceptional point and the value increases with increasing κ. Thus, strong magnetic coupling is desired for large damping rate. However, the CMT deviates from exact solutions of circuit equations when the damping rate is as high as ω_0 [41]. Hence, the deviation of the CMT is expected around the exceptional point in strong coupling regime. Then, we solve circuit equations and compare the results with the CMT, simulation and experimental results.

According to Kirchhoff's law and Ohm's law, we have the following set of equations in the series *RLC* resonators

$$V_n^L + V_n^C + V_n^R = 0 \tag{6a}$$
$$I_n^L = I_n^C = I_n^R \tag{6b}$$
$$V_n^R = R_n I_n^R \tag{6c}$$
$$I_n^c = \frac{dQ_n}{dt} \tag{6d}$$

where V, I, R, C, and L are the voltage, current, resistance, capacitance, and inductance, respectively, and Q is charge in the capacitor. The subscript $n = 1$ or 2 represents the main circuit or external resonator, respectively. From (6a)–(6d) and $\mu \neq 1$, we have the simultaneous differential equations

$$\frac{d^2Q_1}{dt^2} + \frac{\omega_0^2}{1-\mu^2}Q_1 - \frac{\mu\omega_0^2}{1-\mu^2}Q_2 + \frac{\Gamma_1\omega_0}{1-\mu^2}\frac{dQ_1}{dt} - \frac{\mu\Gamma_2\omega_0}{1-\mu^2}\frac{dQ_2}{dt} = 0 \tag{7a}$$

$$\frac{d^2Q_2}{dt^2} + \frac{\omega_0^2}{1-\mu^2}Q_2 - \frac{\mu\omega_0^2}{1-\mu^2}Q_1 + \frac{\Gamma_2\omega_0}{1-\mu^2}\frac{dQ_2}{dt} - \frac{\mu\Gamma_1\omega_0}{1-\mu^2}\frac{dQ_1}{dt} = 0. \tag{7b}$$

Using $\Gamma_n = R_n\sqrt{C_n/L_n}\omega_0 = 1/\sqrt{LC}$, (7a) and (7b) are rewritten as

$$\begin{bmatrix} -\frac{\omega^2}{\omega_0^2} + \frac{i\Gamma_1}{1-\mu^2}\frac{\omega}{\omega_0} + \frac{1}{1-\mu^2} & -\frac{\mu}{1-\mu^2}\left(1 + i\Gamma_2\frac{\omega}{\omega_0}\right) \\ -\frac{\mu}{1-\mu^2}\left(1 + i\Gamma_1\frac{\omega}{\omega_0}\right) & -\frac{\omega^2}{\omega_0^2} + \frac{i\Gamma_2}{1-\mu^2}\frac{\omega}{\omega_0} + \frac{1}{1-\mu^2} \end{bmatrix} \times \begin{pmatrix} Q_1 \\ Q_2 \end{pmatrix} = 0. \tag{8}$$

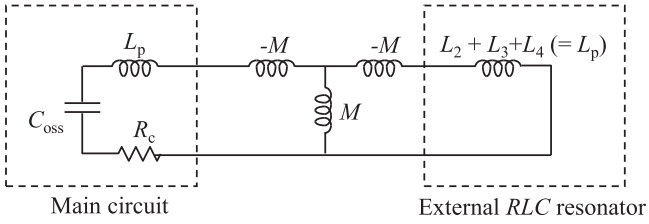

Fig. 2. Equivalent circuit of magnetic coupling when C_2 and R_2 are short-circuited.

From (8), complex eigen frequencies satisfy

$$\left(-\frac{\omega^2}{\omega_0^2} + \frac{i\Gamma_1}{1-\mu^2}\frac{\omega}{\omega_0} + \frac{1}{1-\mu^2}\right)\left(-\frac{\omega^2}{\omega_0^2} + \frac{i\Gamma_2}{1-\mu^2}\frac{\omega}{\omega_0} + \frac{1}{1-\mu^2}\right) - \left[-\frac{\mu}{1-\mu^2}\left(1 + i\Gamma_2\frac{\omega}{\omega_0}\right)\right]\left[-\frac{\mu}{1-\mu^2}\left(1 + i\Gamma_1\frac{\omega}{\omega_0}\right)\right] = 0. \tag{9}$$

We numerically solve (9) around the exceptional point, which is obtained from the CMT.

III. Experiment

First, the magnetic coupling coefficient between the main circuit and the external resonator was deduced by using the equivalent circuit of the magnetically coupled inductance shown in Fig. 2 [39], [40]. L_p is the total inductance of the main circuit ($L_\mathrm{p} = L_0 + L_1 + L_c$), which equals to the inductance when the external resonator is open-terminated. The inductance, when C_2 and R_2 are short-circuited (L_short), is given by

$$L_\mathrm{short} = L_\mathrm{p} - M + \frac{1}{M^{-1} + (L_\mathrm{p} - M)^{-1}}. \tag{10}$$

From (10), the mutual inductance M is given by

$$M = \sqrt{L_\mathrm{p}^2 - L_\mathrm{p}L_\mathrm{short}}. \tag{11}$$

The magnetic coupling coefficient μ is deduced as

$$\mu = \frac{M}{L_\mathrm{p}}. \tag{12}$$

L_p and L_short are deduced from the ringing frequency when the external resonator is open-terminated, and C_2 and R_2 are short-circuited, respectively. The ringing frequencies are $f_\mathrm{p} = 1/2\pi\sqrt{L_\mathrm{p}C_\mathrm{oss}}$ and $f_\mathrm{short} = 1/2\pi\sqrt{L_\mathrm{short}C_\mathrm{oss}}$, respectively.

Then, we retrieved key parameters with the open-terminated external resonator as follows. L_p was obtained from the ringing frequency f_p. The voltage dependence of C_oss was measured with a curve tracer (B1505A, Keysight). R_c was obtained by fitting a ringing voltage waveform with $V \propto \exp[-\gamma_1 t]$ [17]. Then, L_3 was set to be equal to L_0, and L_4 was chosen so that the total inductance of the external resonator equals to L_p by measuring the total inductance with an impedance analyzer (E4980A, Agilent). Next, we obtained a magnetic coupling coefficient from the ringing frequency f_short. Then, C_2 and R_2 were inserted and switching waveforms were obtained varying R_2.

The experimental setup for the double pulse circuit with the *RLC* resonator is shown in Fig. 3. An all-SiC half-bridge module (CAS120M12BM2, Cree, Inc.) [42] was used. A load inductor of 100 μH (LSFHAM-101U100A, Pony Electric Co., LTD) and a

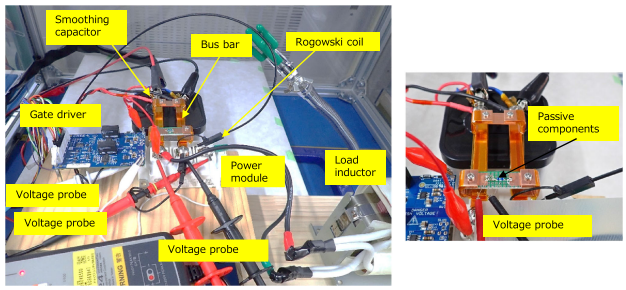

Fig. 3. Experimental setup of the double-pulse circuit with the magnetically coupled bus bar. (a) Perspective view. (b) External resonator.

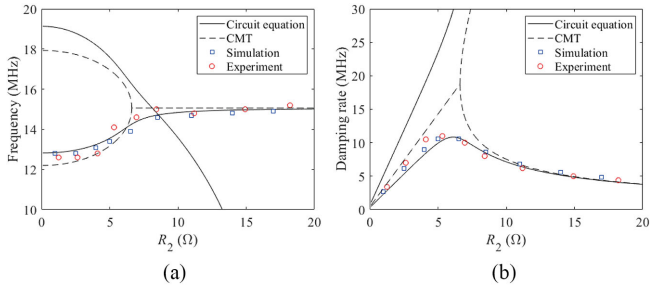

Fig. 4. Parametric evolution of (a) resonance frequencies and (b) damping rates as a function of R_2.

TABLE I
CIRCUIT PARAMETERS

Main circuit		External resonator	
L	100 nH	L_2	70 nH**
C	400 μF	L_3	15 nH
L_0	15 nH*	L_4	6.8 (5.0***) nH
L_p	90 nH**	C_2	1.2 nF
C_{oss}	1.2 nF**	μ	0.38
R_c	140 mΩ**		

*: From data sheet [42].
**: Experimentally determined values.
***: Value for calculation.

TABLE II
PARAMETERS FOR CMT AND CIRCUIT EQUATION

ω_0	9.5×10^7 rad/s
γ_1	7.6×10^5 rad/s
κ	1.8×10^7 rad/s
Γ_1	0.016

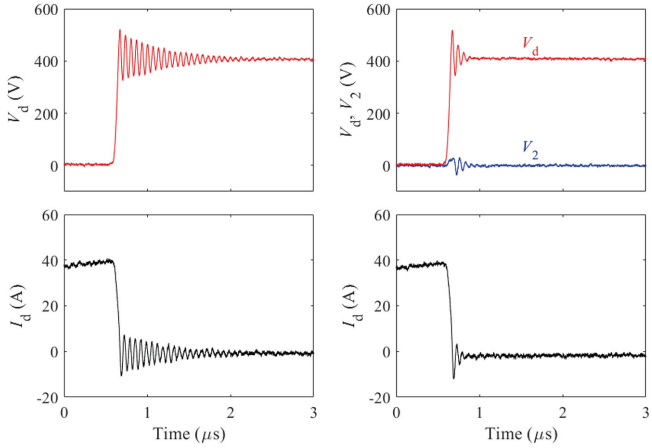

Fig. 5. Experimental switching waveforms of V_d and I_d (a) without and (b) with the external resonator ($R_2 = 5.3\ \Omega$).

smoothing capacitor of 400 μF (MEC-HC, Shizuki Electric Co., Inc.) were used. A gate voltage of $+22/-5$ V was applied using a dual channel gate driver (CGD15HB62P1, Cree, Inc), and the gate signal was applied using a function generator (FC300 Yokogawa Electric Corporation). A source voltage of 400 V was applied by a dc voltage source (HV1.5-1, Takasago LTD). The waveforms of V_d and V_2 were measured by voltage probes (701943, 701944, Yokogawa Electric Corporation). The current was measured with a Rogowski coil (SS-283A, Iwatsu Electric Co., Ltd). The above probes were connected to an oscilloscope (DL9240, Yokogawa Electric Corporation).

The damping rate of ringing α, which is different from the intrinsic damping rate γ_n, was retrieved by fitting the envelope of a time-domain ringing waveform with $V \propto \exp(-\alpha t)$ [10]. The circuit parameters are given in Table I. C_{oss} is the value at 400 V. The corresponding parameters for calculations of CMT and circuit equation are given in Table II. In addition to the experiment, we performed numerical simulations with LTspice XVII.

IV. RESULTS AND DISCUSSIONS

First, we examined eigen frequencies and damping rates for different values of R_2. Then, we investigated switching waveforms and the spectra for specific values of R_2.

Fig. 4 shows the parametric evolution of the resonance frequencies and damping rates as a function of R_2. The measured resonance frequency (circles) gradually increases with increasing R_2 up to 8.4 Ω, and becomes almost constant with further increase of R_2. The measured damping rate (circles) is maximal at $R_2 = 5.3\ \Omega$. The measured results agree well with the simulation results (squares) obtained by LTspice XVII. Although there are two branches in the resonance frequencies and damping rates in the circuit equation results [solid lines, (12)] and the CMT results [dashed lines, (6)], the branch with the low damping rate becomes dominant, as observed in the measured results, because the branch with the high damping rate vanishes more quickly. The circuit equation results agree well with the experimental results with the maximal damping rate around $R_2 \approx 6.0\ \Omega$. The exceptional point obtained by the CMT reasonably estimates the maximum damping rate with $R_2 \approx 6.5\ \Omega$. The deviation between the circuit equation and CMT results around the exceptional point, where the eigen frequencies in the CMT coalesce, comes from strong coupling between the two resonators.

Fig. 5(a) shows the experimental waveform of V_d and drain current I_d without the external resonator. Ringing was observed after the switching operation. Fig. 5(b) shows the experimental waveforms of V_d, V_2, and I_d with the external resonator when R_2 is 5.3 Ω, in which the ringing was sufficiently suppressed. The same behaviors are reproduced by simulation results shown in Fig. 6.

Fig. 7 shows the spectra of the ringing in the experiment. The spectral peak voltage with the external resonator is suppressed to 15% comparing with that without the external resonator.

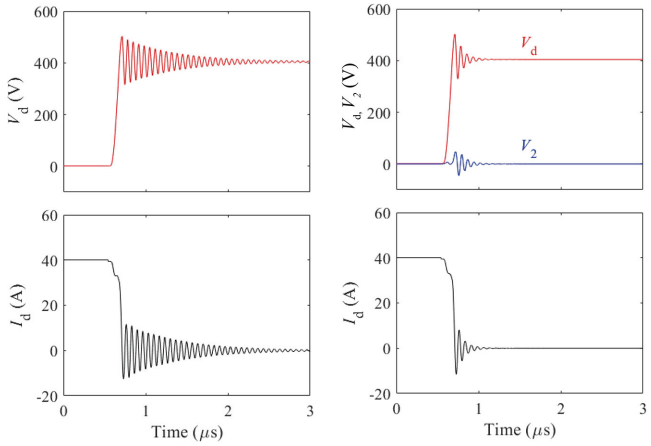

Fig. 6. Simulated switching waveforms of V_d and I_d (a) without and (b) with the external resonator ($R_2 = 5.0\ \Omega$).

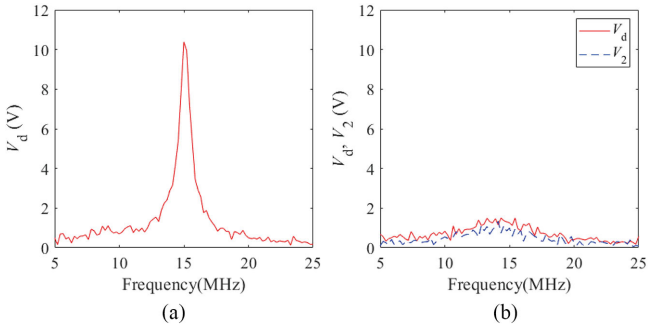

Fig. 7. Experimental spectra of ringing (a) without and (b) with the external resonator ($R_2 = 5.3\ \Omega$).

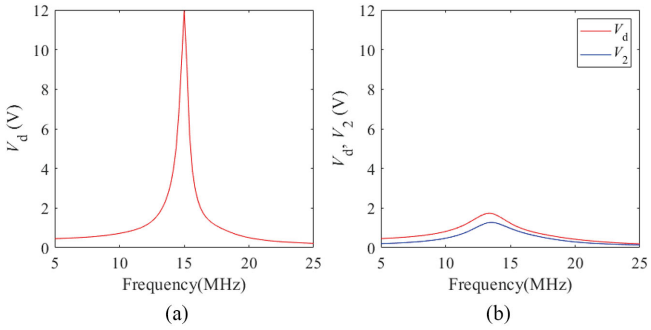

Fig. 8. Simulated spectra of ringing (a) without and (b) with the resonator ($R_2 = 5.0\ \Omega$).

The peak voltage reduction rate is higher than the results of Ref [33]. The high ringing suppression effect comes from the strong magnetic coupling. Our magnetic coupling coefficient of 0.38 is larger than that in [23] (about 0.14). The spectra of V_d and V_2 shown in Fig. 7(b) are almost the same, indicating that ringing energy is effectively distributed to the external resonator, and experienced the loss of the external resonator. The ringing suppression effect and the energy distribution to the external resonator in spectra were confirmed by simulation results shown in Fig. 8.

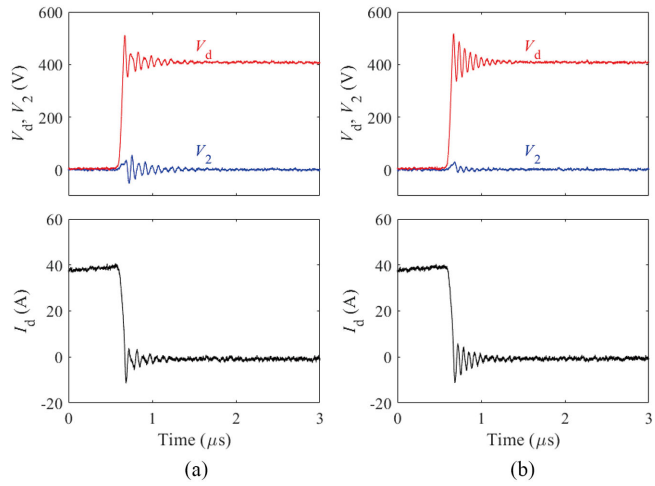

Fig. 9. Experimental switching waveform of V_d and I_d. (a) With $R_2 = 1.3\ \Omega$. (b) With $R_2 = 18.2\ \Omega$.

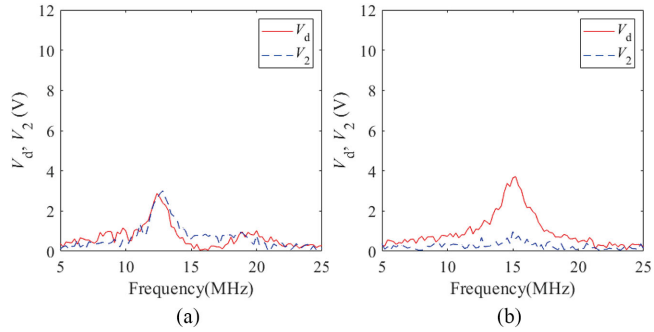

Fig. 10. Experimental spectra of ringing. (a) With $R_2 = 1.3\ \Omega$. (b) With $R_2 = 18.2\ \Omega$.

Fig. 9(a) and (b) shows the waveforms with the external resonator when R_2 is 1.3 and 18.2 Ω, respectively. The ringing continues longer than the case shown in Fig 5(b), and the peak voltage of spectra shown in Fig. 10 is about 30% of the case without the external resonator. On the other hand, the behavior of V_2 is different for the above two cases. Fig. 10(a) and (b) shows the ringing spectra when R_2 is 1.3 and 18.2 Ω, respectively. The peak voltages of V_d and V_2 are almost the same when R_2 is 1.3 Ω. When R_2 is 18.2 Ω, V_2 is smaller than V_d. This behavior is indeed the feature of passive PT symmetry [31]. When the lossy resonator has small loss, the energy is equally distributed between the resonators. Conversely, the total loss is small due to the small loss of the lossy resonator. On the other hand, when the lossy resonator has large loss, the energy is less likely to be distributed between the resonators, which results in that the energy is less likely to experience the loss. We note that the system is in the unbroken phase for $R_2 = 1.3, 5.3\ \Omega$, or in the broken phase for $R_2 = 18.2\ \Omega$ in passive PT-symmetry.

The switching loss is calculated through the integration of $V_d \times I_d$ in time using 10% limits of V_d and I_d. The switching losses with and without the *RLC* resonator were 0.32 and 0.33 mJ, respectively. The external resonator hardly affects the

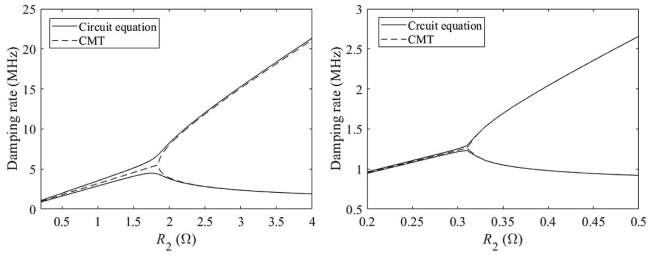

Fig. 11. Damping rates as a function of resistance R_2 obtained by circuit equation and CMT in weak coupling condition. (a) $\mu = 0.1$, (b) $\mu = 0.01$.

switching loss. In addition to the switching loss, we discuss the current ripple loss at the circuit operation frequency and damped energy in the external resonator. As for the current ripple loss, the additive impedance by the external resonator Z(s) is expressed as [23]

$$\mathrm{Z}(j\omega) = \frac{-(j\omega)^3 M^2 C_2}{(j\omega)^2 (L_2 + L_3 + L_4) C_2 + j\omega R_2 C_2 + 1}. \quad (13)$$

The operation frequency of the power converter circuit is generally as high as few tens of kilohertz. The real part of $Z(j\omega)$ in the range of few tens of kilohertz is as low as $\sim 10^{-11}$ (Ω). Thus, the external resonator has little effect on the ripple loss. As for damped energy in the external resonator, we calculated the loss by integrating $R_2 I_2^R 2$ in time for $R_2 = 5.0\ \Omega$. The external resonator has a loss of 8.4 μJ, which is negligibly small comparing with the switching loss. Considering together with the current ripple loss, the external resonator has little effect on circuit efficiency. Our configuration using the external resonator has higher circuit efficiency comparing with typical *RC*-circuits inserted in parallel with switching devices since *RC*-circuits often increase switching loss [10].

The discrepancies of the CMT results (dashed lines) from the circuit equation results (solid lines) in damping rate near the exceptional point arise from the strong coupling, as mentioned in Fig. 4. On the other hand, the system characteristics can be well described by the CMT when the coupling is weak. Fig. 11 shows the damping rates as a function of R_2 for weak coupling condition. The circuit equation results (9) get close to the results obtained by the CMT (3), and the lower damping rate is maximal around the exceptional point. Thus, we have proved that the CMT provides a reasonable estimation of resistance R_2 with physical insight for optimal design of our system even in strong coupling regime although a discrepancy occurs.

V. Conclusion

We have shown that parasitic ringing can be significantly suppressed by implementing an external resonator in parallel to the bus bar through analogy with passive PT-symmetry. Owing to the strong coupling enabled by putting the bus bars in parallel, the peak voltage of ringing decreased to 15% of the original waveform. Ringing was suppressed through analogy with passive PT-symmetry, i.e., the ringing energy is effectively distributed to the external resonator when the external resonator has small loss, and the ringing energy is less likely to be distributed to the external resonator when the external resonator has large loss. We showed that the passive PT symmetry analogy can be extended to strong coupling regime. Our results represent a significant step toward practical applications of passive PT-symmetry.

Appendix

Here, we show the derivation of (7). The V_n^L, V_n^C and V_n^R are expressed as

$$V_1^L = L_1 \frac{dI_1^L}{dt} + M \frac{dI_2^L}{dt} \quad (A1a)$$

$$V_2^L = L_2 \frac{dI_2^L}{dt} + M \frac{dI_1^L}{dt} \quad (A1b)$$

$$V_n^C = \frac{Q_n}{C_n} \quad (A1c)$$

$$V_n^R = R_n I_n^R. \quad (A1d)$$

Inserting (A1) into (6a), we have the simultaneous equations

$$L_1 \frac{dI_1^L}{dt} + M \frac{dI_2^L}{dt} + \frac{Q_1}{C_1} + R_1 I_1^R = 0 \quad (A2a)$$

$$L_2 \frac{dI_2^L}{dt} + M \frac{dI_1^L}{dt} + \frac{Q_2}{C_2} + R_2 I_2^R = 0. \quad (A2b)$$

Using (6b) and (6d), (A2) are rewritten as

$$L_1 \frac{d^2 Q_1}{dt^2} + M \frac{d^2 Q_2}{dt^2} + \frac{Q_1}{C_1} + R_1 \frac{dQ_1}{dt} = 0 \quad (A3a)$$

$$L_2 \frac{d^2 Q_2}{dt^2} + M \frac{d^2 Q_1}{dt^2} + \frac{Q_2}{C_2} + R_2 \frac{dQ_2}{dt} = 0. \quad (A3b)$$

In our case, we have $C_1 = C_2$ and $L_1 = L_2$. Thus, $\omega_0 = 1/\sqrt{L_1 C_1} = 1/\sqrt{L_2 C_2}$ and $\mu = M/\sqrt{L_1 L_2} = M/L_1 = M/L_2$. Equation (A3) are then expressed as

$$\frac{d^2 Q_1}{dt^2} + \mu \frac{d^2 Q_2}{dt^2} + \omega_0^2 Q_1 + \Gamma_1 \omega_0 \frac{dQ_1}{dt} = 0 \quad (A4a)$$

$$\frac{d^2 Q_2}{dt^2} + \mu \frac{d^2 Q_1}{dt^2} + \omega_0^2 Q_2 + \Gamma_2 \omega_0 \frac{dQ_2}{dt} = 0. \quad (A4b)$$

From (A4), (7a) and (7b) are obtained.

References

[1] J. M Carrasco, L. G. Franquelo, J. T. Bialasiewicz, E. Galvan, M. A. M. Prats, J. I. Leon, and N. Moreno-Alfonso, "Power-electronic systems for the grid integration of renewable energy sources: A survey," *IEEE Trans. Ind. Electron.*, vol. 53, no. 4, pp. 1002–1016, Jun. 2006.

[2] J. H. Feng, W. Q. Chu, Z. X. Zhang, and Z. Q. Zhu, "Power electronic transformer-based railway traction systems: Challenges and opportunities," *IEEE Trans. Emerg. Sel. Top. Power Electron.*, vol. 5, no. 3, pp. 1237–1253, Sep. 2017.

[3] S. S. Williamson, A. K. Rathore, and F. Musavi, "Industrial electronics for electric transportation: Current state-of-the-art and future challenges," *IEEE Trans. Ind. Electron.*, vol. 62, no. 5, pp. 3021–3032, May 2015.

[4] J. Falck, C. Felgemacher, A. Rojko, M. Liserre, and P. Zacharias, "Reliability of power electronic systems: An industry perspective," *IEEE Ind. Electron. M.*, vol. 12, no. 2, pp. 24–35, Jun. 2018.

[5] J. Millan, P. Godignon, X. Perpina, A. Perez-Tomas, and J. Rebollo, "A survey of wide bandgap power semiconductor devices," *IEEE Trans. Power Electron.*, vol. 29, no. 5, pp. 2155–2163, May 2014.

[6] D. Han, J. Noppakunkajorn, and B. Sarlioglu, "Comprehensive efficiency, weight, and volume comparison of SiC- and Si-based bidirectional DC-DC converters for hybrid electric vehicles," *IEEE Trans. Veh. Technol.*, vol. 63, no. 7, pp. 3001–3010, Sep. 2014.
[7] X. She, A. Q. Huang, O. Lucia, and B. Ozpineci, "Review of silicon carbide power devices and their applications," *IEEE Trans. Ind. Electron.*, vol. 64, no. 10, pp. 8193–8205, Oct. 2017.
[8] M. Imaizumi and N. Miura, "Characteristics of 600, 1200, and 3300 V planar SiC-MOSFETs for energy conversion applications," *IEEE Trans. Electron Devices*, vol. 62, no. 2, pp. 390–395, Feb. 2015.
[9] Z. Liang, P. Ning, and F. Wang, "Development of advanced all-SiC power modules," *IEEE Trans. Power Electron.*, vol. 29, no. 5, pp. 2289–2295, May 2014.
[10] T. J. Liu, T. T. Y. Wong, and Z. J. Shen, "A survey on switching oscillations in power converters," *IEEE Trans. Emerg. Sel. Top. Power Electron.*, vol. 8, no. 1, pp. 893–908, Mar. 2020.
[11] T. J. Liu, R. T. Ning, T. T. Y. Wong, and Z. J. Shen, "Modeling and analysis of SiC MOSFET switching oscillations," *IEEE Trans. Emerg. Sel. Top. Power Electron.*, vol. 4, no. 3, pp. 747–756, Sep. 2016.
[12] Z. Chen, Y. Y. Yao, D. Boroyevich, K. D. T. Ngo, P. Mattavelli, and K. Rajashekara, "A 1200-V, 60-A SiC MOSFET multichip phase-leg module for high-temperature, high-frequency applications," *IEEE Trans. Power Electron.*, vol. 29, no. 5, pp. 2307–2320, May 2014.
[13] Z. Zeng and X. Li, "Comparative study on multiple degrees of freedom of gate drivers for transient behavior regulation of SiC MOSFET," *IEEE Trans. Power Electron.*, vol. 33, no. 10, pp. 8754–8763, Oct. 2018.
[14] B. Y. Zhang and S. Wang, "A survey of EMI research in power electronics systems with wide-bandgap semiconductor devices," *IEEE Trans. Emerg. Sel. Top. Power Electron.*, vol. 8, no. 1, pp. 626–643, Mar. 2020.
[15] N. Oswald, P. Anthony, N. McNeill, and B. H. Stark, "An experimental investigation of the tradeoff between switching losses and EMI generation with hard-switched all-Si, Si-SiC, and All-SiC device combinations," *IEEE Trans. Power Electron.*, vol. 29, no. 5, pp. 2393–2407, May 2014.
[16] D. Han and B. Sarlioglu, "Comprehensive study of the performance of SiC MOSFET-based automotive DC–DC converter under the influence of parasitic inductance," *IEEE Trans. Ind. Appl.*, vol. 52, no. 6, pp. 5100–5111, Nov./Dec. 2016.
[17] K. Yatsugi, K. Nomura, and Y. Hattori, "Analytical technique for designing an RC snubber circuit for ringing suppression in a phase-leg configuration," *IEEE Trans. Power Electron.*, vol. 33, no. 6, pp. 4736–4745, Jun. 2018.
[18] A. Garcia-Caraveo, A. Soto, R. Gonzalez, and P. Banuelos-Sanchez, "Brief review on snubber circuits," in *Proc. 20th Int. Conf. Electron. Commun. Comput.*, 2010, pp. 271–275.
[19] R. A. Wood and T. E. Salem, "Evaluation of a 1200-V, 800-A All-SiC dual module," *IEEE Trans. Power Electron.*, vol. 26, no. 9, pp. 2504–2511, Sept. 2011.
[20] M. J. Pan and C. A. Randall, "A brief introduction to ceramic capacitors," *IEEE Elect. Insul. Mag.*, vol. 26, no. 3, pp. 44–50, May/Jun 2010.
[21] I. Josifović, J. Popović-Gerber, and J. A. Ferreira, "Improving SiC JFET switching behavior under influence of circuit parasitics," *IEEE Trans. Power Electron.*, vol. 27, no. 8, pp. 3843–3854, Aug. 2012.
[22] A. Teverovsky, "Breakdown voltages in ceramic capacitors with cracks," *IEEE Trans. Dielect. Elect. Insul.*, vol. 19, no. 4, pp. 1448–1455, Aug. 2012.
[23] H. Wang and F. Blaabjerg, "Reliability of capacitors for DC-link applications in power electronic converters—An overview," *IEEE Trans. Ind. Appl.*, vol. 50, no. 5, pp. 3569–3578, Sep/Oct. 2014.
[24] L. Feng, R. El-Ganainy, and L. Ge, "Non-Hermitian photonics based on parity-time symmetry," *Nature Photon.*, vol. 11, no. 12, pp. 752–762, Dec. 2017.
[25] S. K. Ozdemir, S. Rotter, F. Nori, and L. Yang, "Parity-time symmetry and exceptional points in photonics," *Nature Mater.*, vol. 18, no. 8, pp. 783–798, Aug. 2019.
[26] D. L. S. R. Fleury, A. Alù, "Parity-time symmetry in acoustics: Theory, devices, and potential applications," *IEEE J. Sel. Top. Quantum Electron.*, vol. 22, no. 5, pp. 121–129, Sep/Oct. 2016.
[27] R. Fleury, D. Sounas, and A. Alu, "An invisible acoustic sensor based on parity-time symmetry," *Nature Commun.*, vol. 6, Jan. 2015, Art. no. 5905.
[28] J. Schindler, A. Li, M. C. Zheng, F. M. Ellis, and T. Kottos, "Experimental study of active LRC circuits with PT symmetries," *Phys. Rev. A*, vol. 84, no. 4, Oct. 2011, Art. no. 040101.
[29] P. Y. Chen *et al.*, "Generalized parity-time symmetry condition for enhanced sensor telemetry," *Nature Electron.*, vol. 1, no. 5, pp. 297–304, May 2018.
[30] S. Assawaworrarit, X. F. Yu, and S. H. Fan, "Robust wireless power transfer using a nonlinear parity-time-symmetric circuit," *Nature*, vol. 546, no. 7658, pp. 387–390, Jun. 2017.
[31] A. Guo *et al.*, "Observation of PT-Symmetry breaking in complex optical potentials," *Phys. Rev. Lett.*, vol. 103, no. 9, Aug. 2009.
[32] M. Ornigotti and A. Szameit, "Quasi PT-symmetry in passive photonic lattices," *J. Opt.*, vol. 16, no. 6, Jun. 2014.
[33] J. Kim, D. Shin, and S. K. Sul, "A damping scheme for switching ringing of full SiC MOSFET by Air core PCB circuit," *IEEE Trans. Power Electron.*, vol. 33, no. 6, pp. 4605–4615, Jun 2018.
[34] T. Funk and B. Wicht, "A fully integrated DC to 75 MHz current sensing circuit with on-chip rogowski coil," in *Proc. IEEE Custom Integr. Circuits Conf.*, 2018, pp. 1–4.
[35] M. H. Samimi, A. Mahari, M. A. Farahnakian, and H. Mohseni, "The rogowski coil principles and applications: A review," *IEEE Sens. J.*, vol. 15, no. 2, pp. 651–658, Feb. 2015.
[36] M. Shafiq, L. Kutt, M. Lehtonen, T. Nieminen, and M. Hashmi, "Parameters identification and modeling of high-frequency current transducer for partial discharge measurements," *IEEE Sens. J.*, vol. 13, no. 3, pp. 1081–1091, Mar. 2013.
[37] V. Dubickas and H. Edin, "High-frequency model of the Rogowski coil with a small number of turns," *IEEE Trans. Instrum. Meas.*, vol. 56, no. 6, pp. 2284–2288, Dec. 2007.
[38] R. El-Ganainy, K. G. Makris, M. Khajavikhan, Z. H. Musslimani, S. Rotter, and D. N. Christodoulides, "Non-Hermitian physics and PT symmetry," *Nature Phys.*, vol. 14, no. 1, pp. 11–19, Jan. 2018.
[39] K. Sasaki, S. Sugiura, and H. Iizuka, "Distance adaptation method for magnetic resonance coupling between variable capacitor-loaded parallel-wire coils," *IEEE Trans. Microw. Theory Tech.*, vol. 62, no. 4, pp. 892–900, Apr. 2014.
[40] T. Imura and Y. Hori, "Maximizing Air Gap and efficiency of magnetic resonant coupling for wireless power transfer using equivalent circuit and neumann formula," *IEEE Trans. Ind. Electron.*, vol. 58, no. 10, pp. 4746–4752, Oct. 2011.
[41] H. A. Haus, *Waves and fields in optoelectronics*. Englewood Cliffs, NJ, USA: Prentice-Hall, 1984, ch. 7.
[42] CAS120M12BM2 1.2kV, 13mΩAll-silicon carbide half-bridge module. Cree, Inc. Durham, NC, USA, 2014.

Kenichi Yatsugi received the M.S. degree in applied physics from Osaka University, Osaka, Japan, in 2012.

He joined Toyota Central R&D Labs., Inc., in 2012. His current research interests include developments of electromagnetic devices for automotive applications.

Mr. Yatsugi is a member of the Japan Society of Applied Physics.

Koshi Oishi received the B.E. degree in information and image engineering and the M.E. degree in information science from Chiba University, Chiba, Japan, in 2010 and 2012, respectively.

He joined Toyota Central R&D Labs., Inc., in 2012. His current research interests include digital circuit design and robotic systems.

Hideo Iizuka (Member, IEEE) received the B.S. and the M.S. degrees in electrical engineering from Saitama University, Saitama, Japan, in 1995 and 1997, respectively, and the Ph.D. degree in engineering from Nagoya Institute of Technology, Nagoya, Japan, in 2007.

In 1997, he joined Toyota Central R&D Labs., Inc., Nagakute, Japan. From 2001 to 2002, he was a Visiting Scholar with the University of Birmingham, Birmingham, U. K. From 2008 to 2011 and since 2017, he has been with Toyota Research Institute of North America, Toyota Motor North America, Inc., Ann Arbor, MI, USA. His research interests include analyses and developments of devices and subsystems in electromagnetics and acoustics.